



**HAL**  
open science

# Characterization of Bubble Shapes in Non-Newtonian Fluids by Parametric Equations

Feishi Xu, Noel Midoux, Huai-Zhi Li, Gilles Hébrard, Nicolas Dietrich

► **To cite this version:**

Feishi Xu, Noel Midoux, Huai-Zhi Li, Gilles Hébrard, Nicolas Dietrich. Characterization of Bubble Shapes in Non-Newtonian Fluids by Parametric Equations. *Chemical Engineering and Technology*, 2019, 42 (11), pp.2321-2330. 10.1002/ceat.201800690 . hal-02274472

**HAL Id: hal-02274472**

**<https://hal.science/hal-02274472v1>**

Submitted on 22 Nov 2019

**HAL** is a multi-disciplinary open access archive for the deposit and dissemination of scientific research documents, whether they are published or not. The documents may come from teaching and research institutions in France or abroad, or from public or private research centers.

L'archive ouverte pluridisciplinaire **HAL**, est destinée au dépôt et à la diffusion de documents scientifiques de niveau recherche, publiés ou non, émanant des établissements d'enseignement et de recherche français ou étrangers, des laboratoires publics ou privés.

# 1 CHARACTERIZATION OF BUBBLE SHAPES IN NON-NEWTONIAN FLUIDS BY 2 PARAMETRIC EQUATIONS

3

4 Feishi Xu<sup>1</sup>, Noel Midoux<sup>2</sup>, Huai-Zhi Li<sup>2</sup>, Gilles Hébrard<sup>1</sup> and Nicolas Dietrich<sup>1,\*</sup>

5 <sup>1</sup>Laboratoire d'Ingénierie des Systèmes Biologiques et des Procédés (LISBP), Université de  
6 Toulouse, CNRS, INRA, INSA, 135 Avenue de Rangueil, 31077 Toulouse, France

7 <sup>2</sup>Laboratoire Réactions et Génie des Procédés (LRGP), Université de Lorraine, CNRS, 1 rue  
8 Grandville, BP 20451, 54001 Nancy Cedex, France

9 Email corresponding author: [dietrich@insa-toulouse.fr](mailto:dietrich@insa-toulouse.fr)

10

## 11 **Abstract**

12 Based on the experiment of single air bubbles rising in stagnant non-Newtonian fluids, an  
13 innovative model containing the aspect ratio ( $E$ ) and two parameters ( $\alpha$ ,  $\beta$ ) was proposed  
14 and proved to be capable of characterizing the bubble shape from spherical/ellipsoidal to  
15 prolate/oblate-tear with good accuracy. Several impacts on bubble deformation were  
16 investigated involving the rheological properties of the fluids and different forces exerted on  
17 the bubble which were quantified by multiple dimensionless numbers (e.g. Reynolds number,  
18 Eötvös Number, Deborah number). Within a wide range ( $-9 < \log Mo < 3$ ,  $Mo$ : Morton number),  
19 the empirical correlations were obtained for parameter  $\beta$ , and between  $\alpha$  and  $\beta$ . Together  
20 with the shape model, a complete system was set up for bubble shape characterization and  
21 prediction that will provide new ideas for future studies on bubble hydrodynamics.

22

23 **Keywords: Bubble shape, Bubble dynamics, Gas-liquid system, Non-Newtonian fluid**

24

## 25 **1 Introduction**

26 Bubble-liquid systems are widespread in industries such as oil extraction, wastewater  
27 treatment and bioreactors. For these applications, the knowledge of bubble shape is of  
28 importance since it is directly related to hydrodynamic behavior (e.g. terminal velocity, drag,  
29 surface area) and can influence the mixing level and the efficiency of energy, mass, and  
30 momentum transfer.

31 The observed shapes of individual bubbles in free motion in Newtonian fluids have been well  
32 investigated and can be divided mainly into three categories: spherical, ellipsoidal, and  
33 spherical-cap or ellipsoidal-cap [1,2]. Grace et al. [3] have proposed a generalized graphical  
34 correlation or the so-called "Grace diagram" that delineates the shapes of bubbles in  
35 Newtonian fluids, which provides a guideline for the further studies on the bubble shape [4–6].

36 On the other hand, although numerous studies deal with bubbles rising in non-Newtonian  
37 media, only a few of them have discussed and analyzed the bubble shape [7–12]. It is  
38 generally agreed that non-Newtonian fluids have complex rheological properties (e.g. shear  
39 thinning, viscoelasticity, etc.) leading to a variety of bubble shapes, such as teardrop or  
40 elongate bubbles [13–18].

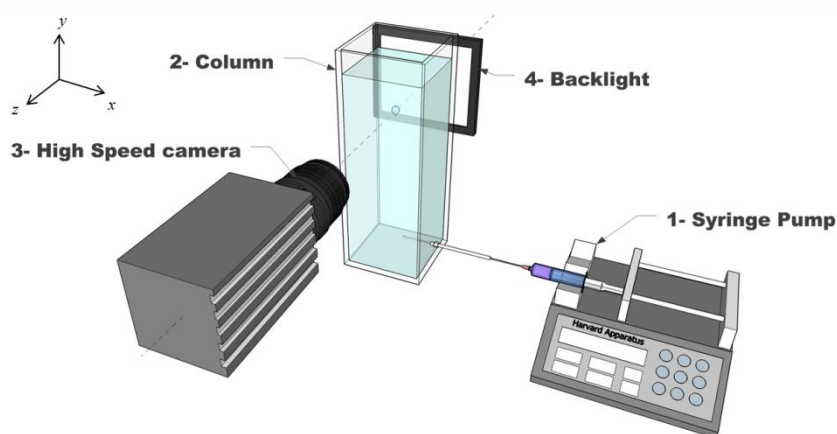
41 To quantitatively characterize the bubble shape, many researchers used the aspect ratio or  
42 eccentricity i.e. the ratio between the lengths of the major and minor axes of the bubbles.  
43 Pioneering work by Moore [19] and Tadaki and Maeda [20] theoretically correlated the  
44 aspect ratio of the bubble with the Weber number and original Tadaki number ( $Ta =$   
45  $Re \cdot Mo^{0.23}$ ), respectively. Their correlation were modified and improved for small inertial  
46 effects [21] and became applicable to clean and contaminated bubbles [22–24] for a large  
47 range of Morton numbers [25]. More recently, many researchers have begun to realize that,  
48 for fluids with high viscosity, no single dimensionless number ( $Eu$ ,  $We$ , or  $Ta$  number) is  
49 suitable to predict the bubble deformation. Therefore, more dimensionless numbers have  
50 been used and many empirical models have been built to fit the results of the new  
51 experiments or numerical simulations [25–28]. For instance, Liu et al. [29] suggested that, in  
52 highly viscous fluids, the bubble shape is dramatically affected by the viscosity and the  
53 effects of  $We$  should be considered along with  $Re$ . However, the aspect ratio suffers from the  
54 shortcoming of being unable to characterize the details of shape or irregular forms (e.g. a  
55 cap bubble and an ellipsoidal bubble would have the same aspect ratio). A few researchers  
56 have tried to use other parameters to characterize the bubble deformation. Myint et al. [30]  
57 introduced a distortion factor to quantify the asymmetry between the upper and lower parts of  
58 the bubble divided by the major axis. Another study, by Yan and Zhao [31], used the bubble  
59 circularity, defined as the ratio of the circumference of an equivalent circle to that of the real  
60 bubble projection. Although some valuable conclusions have been drawn from the previous  
61 work, most of the expressions mentioned above could only handle quasi-ellipsoidal bubbles.  
62 For a bubble with a more complicated contour (e.g. cap, teardrop), it is clear that neither the  
63 aspect ratio nor the circularity can properly characterize the bubble shape.

64 Therefore, in this paper, a new model using the parametric equations is proposed to directly  
65 depict the complete profile of the bubble. Experiments will be implemented to study individual  
66 air bubbles of different sizes (equivalent diameters: 0.7-7 mm) rising in stagnant non-  
67 Newtonian fluids (aqueous solution of polyacrylamide or Xanthan gum) by means of high-  
68 speed photography and image post-processing technologies. The objective mainly aims to  
69 investigate the overall impact (including the different dimensionless numbers and the  
70 rheological properties of the fluid) on the bubble shape.

## 72 2 Materials and method

### 73 2.1 Experimental setup

74 The experimental setup for studying bubble shapes is shown in **Figure 1**. A column (volume:  
75  $100 \times 100 \times 300 \text{ mm}^3$ ) was filled with 2 L of the liquid under study. A single bubble was  
76 generated by injecting the air into the column through a horizontal nozzle located 20 mm  
77 above the column bottom by a syringe pump (Harvard Apparatus, PHD 22/2000) with the  
78 flow rate of  $10 \mu\text{L/h}$ . Stainless steel nozzles of different calibers ( $\approx 0.5\text{-}1 \text{ mm}$ ) were used to  
79 make bubbles of different sizes (equivalent diameters:  $0.7\text{-}7 \text{ mm}$ ). A high-speed camera  
80 (Photon SA3, resolution:  $1024 \times 1024$  pixels) was placed next to one side of the column and  
81 focused on the rising bubble with a vertical image area ( $\approx 40 \times 40 \text{ mm}^2$ ). The recording rate of  
82 the bubble images was 2000 frames per second. The image area was illuminated by a  
83 backlight board placed at the opposite side of the column. The images acquired by the  
84 camera were transmitted to the computer and processed with a professional software (PFV-  
85 Photron FASTCAM Viewer). All the experiments were performed at  $293.15 \text{ K}$  and under  
86 atmospheric pressure.



87

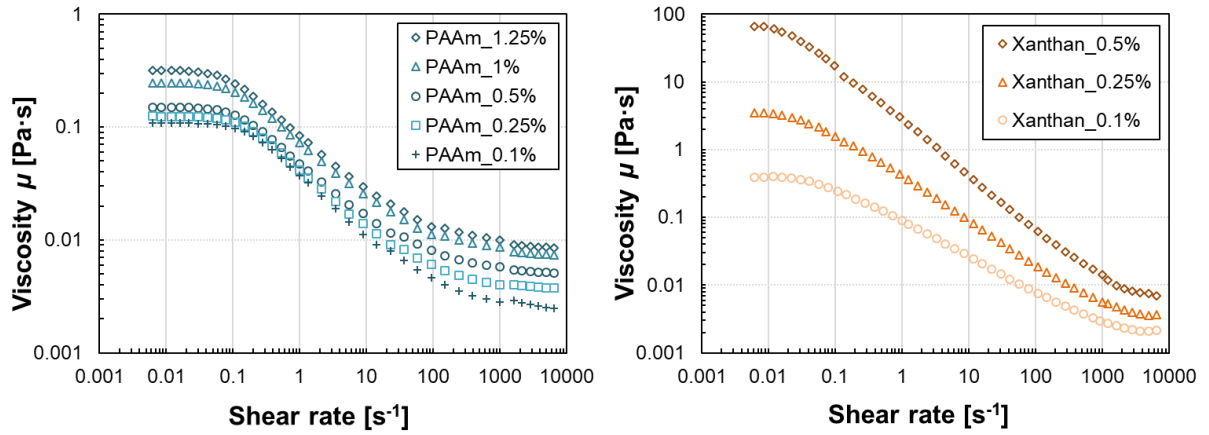
88 **Figure 1.** Experimental setup for bubble shape investigation.

89

### 90 2.2 Materials and the rheological properties

91 Two typical non-Newtonian solutions that are widely used in industries [32] were chosen for  
92 the experiments: poly(acrylamide-co-acrylic acid) partial sodium salt (PAAm) (Sigma-Aldrich,  
93 CAS: 62649-23-4) and Xanthan gum (Sigma-Aldrich, CAS: 11138-66-2). The solutions were  
94 prepared by dissolving powder of substances in deionized water, under five concentrations  
95 for PAAm (0.1%, 0.25 %, 0.5%, 1%, 1.25 % wt.) and three for Xanthan gum (0.1 %, 0.25 %,  
96 0.5% wt.).

97



98

99 **Figure 2.** Flow curves (viscosity versus shear rate) for PAAm solutions and Xanthan gum  
 100 solutions

101

102 The rheological properties of both PAAm and Xanthan solutions were measured by a  
 103 rheometer (HAKKE MARS III, Germany) at 293.15 K with the shear rates ranging from 0.001  
 104  $s^{-1}$  to 10000  $s^{-1}$ . The measured flow curves are plotted in Figure 2. It is found that Xanthan  
 105 solutions have much higher viscosity than that of the PAAm solutions, especially at low shear  
 106 rates ( $<10 s^{-1}$ ). Meanwhile, both of the two solutions present a similar flow behavior. Under  
 107 low and high shear rates, the viscosity approaches a Newtonian plateau where the value of  
 108 viscosity trends to be constant. Between these two plateaus, the viscosity decreases with  
 109 higher shear rate which is known as the shear-thinning property. This evolution can be  
 110 characterized by the classic Carreau model [33,34]:

111 
$$\frac{\mu - \mu_{\infty}}{\mu_0 - \mu_{\infty}} = [1 + (\lambda\dot{\gamma})^2]^{\frac{n-1}{2}} \quad (1)$$

112 where:

- 113
- 114 •  $\mu$  is the variable viscosity [Pa·s];
  - 115 •  $\mu_0$  is the viscosity at the zero shear rate [Pa·s];
  - 116 •  $\mu_{\infty}$  is the viscosity at the infinite shear rate [Pa·s];
  - 117 •  $\dot{\gamma}$  is the variable shear rate [ $s^{-1}$ ];
  - 118 •  $\lambda$  is the relaxation time [s];
  - $n$  is the power index.

119 For each solution under different concentrations, multiple samples were tested and fitted with  
 120 the Carreau model. The fitting results are agreement with the experimental ones with the  
 121 determination coefficient  $r^2 > 97\%$ , proving that the Carreau model is suitable for describing  
 122 the viscosity variation of the investigated non-Newtonian fluids in our cases. The averaged  
 123 results of the regression of the viscosity are shown in Table 1 as well as other general  
 124 physical properties. In this study, the shear rate  $\dot{\gamma}$  near the bubble was estimated by  $\dot{\gamma} =$   
 125  $U/D_{eq}$  with the experimental data: bubble rising velocity  $U$  and equivalent diameter  $D_{eq}$ . This

126 is the characteristic shear rate near the equator of a spherical bubble. The effective shear  
 127 rate may be slightly different for large, non-spherical bubbles, but for simplicity we use the  
 128 same definition in all cases [35]. The methods for calculating  $U$  and  $D_{eq}$  are presented in  
 129 **Section 2.3** and **Section 2.4.1**.

130

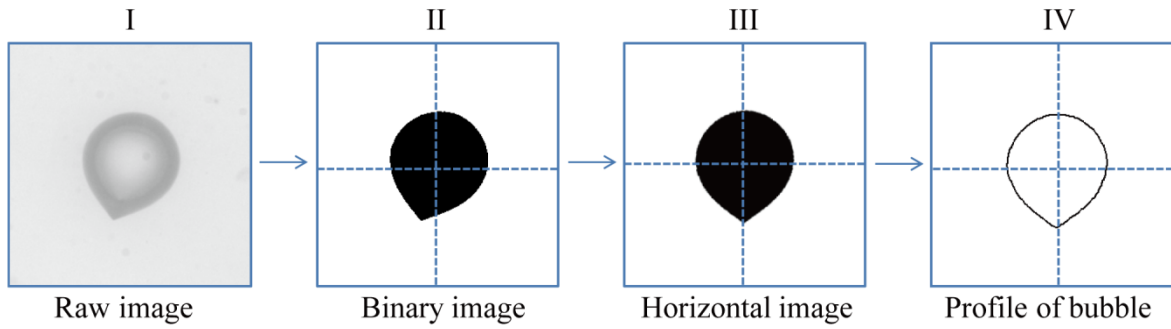
131 **Table 1.** Materials and their physical properties ( $T = 293.15$  K; the viscosity is valid for the  
 132 shear rate ranging between  $0.001 \text{ s}^{-1}$  and  $1000 \text{ s}^{-1}$ ).

Composition	Concentration [wt.]	$\sigma$ [mN/m]	$\rho$ [kg/m <sup>3</sup> ]	$\mu_0$ [Pa·s]	$\mu_\infty$ [Pa·s]	$\lambda$ [s]	$n$
PAAM	0.1%	69	998	0.109	0.003	5.91	0.38
	0.25%	67	999	0.115	0.004	6.77	0.40
	0.5%	66	1000	0.120	0.005	8.19	0.42
	1%	65	1003	0.146	0.007	9.18	0.42
	1.25%	65	1004	0.159	0.008	11.86	0.43
Xanthan	0.1%	69	998	0.36	0.001	15.12	0.47
	0.25%	67	999	3.6	0.002	26.11	0.33
	0.5%	66	1001	69	0.004	59.26	0.20

133

### 134 2.3 Image processing

135 The raw images recorded from the experiment cannot be used directly for the bubble shape  
 136 optimization. An image processing procedure was implemented in MATLAB (R2017b) to  
 137 extract the bubble profile from the raw images. The specific steps are displayed in **Figure 3**.  
 138 Firstly, a reference image concerning the background, which was taken before the passage  
 139 of the bubble, was subtracted from the raw image (**Figure 3-I**). The image thus obtained was  
 140 then transformed into a binary image (**Figure 3-II**) on which the bubble was depicted by a  
 141 black spot after the background noise being removed. Since the bubble may slants while  
 142 rising in the liquid, a rotation was implemented to situate the major axis of the bubble along  
 143 the vertical direction. The bubble profile (**Figure 3-IV**) was finally extracted by recognizing  
 144 the edge of the bubble spot (**Figure 3-III**).



145  
146 **Figure 3.** Schematic views of the image processing steps (Example of a bubble rising in 0.5%  
147 wt. Xanthan solution).

148

149 To calculate the velocity of the bubble, the centroid  $(x_i, y_i)$  of the bubble spot in each frame of  
150 image (**Figure 3-II**) was recognized. Then the distance between the centroids in two  
151 successive frames was divided by the time interval  $\Delta t$  (1/2000 s), thus giving the rising  
152 velocity of the bubble:

153 
$$U = \frac{\sqrt{(x_{i+1}-x_i)^2+(y_{i+1}-y_i)^2}}{\Delta t} \quad (2)$$

154 For a given experimental condition, the averaged values of  $U$  were calculated by considering  
155 20 pairs of images, and the standard deviation is smaller than 1.25%. Herein it can be  
156 assumed that the velocity on the image area has attained the terminal velocity.

157 After the image processing, the bubble profile is put in the Cartesian coordinates making the  
158 bottom of the bubble coincide with the origin and the major axis of the bubble along the  
159 ordinate (see **Figure 4-I**). The coordinates of each point of the bubble profile were then  
160 detected to fit the parametric equations which will be discussed in next section.

161

## 162 **2.4 Characterization of bubble shapes**

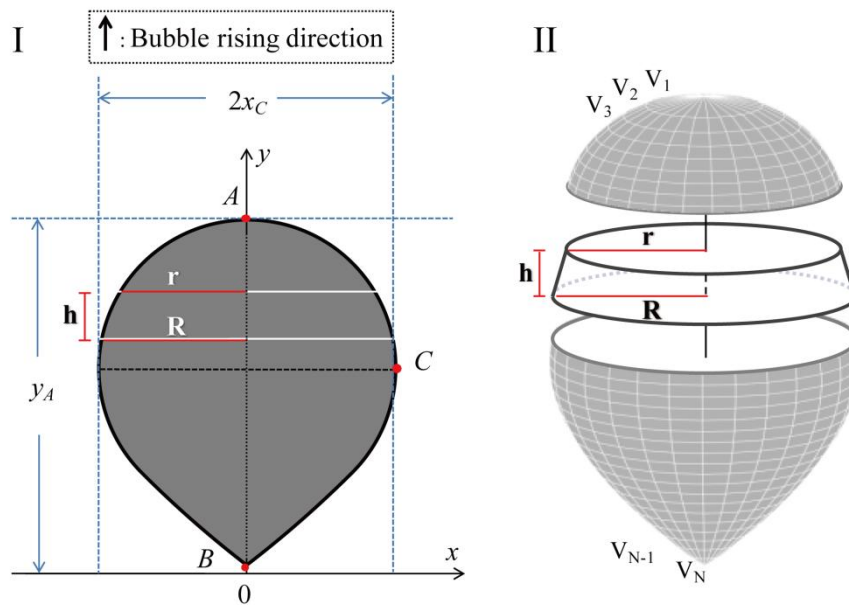
### 163 **2.4.1 Equivalent diameter of the bubble**

164 As shown in **Figure 4-I**, the images obtained from the experiment were two-dimensional  
165 bubble profiles. To calculate the equivalent diameter of the bubble, a reconstruction of the  
166 three-dimensional bubble was implemented considering that the bubble shape was  
167 axisymmetric with respect to the major axis of the bubble profile. Then the 3D bubble was  
168 divided into a set of multiple small circular truncated cones (**Figure 4-II**). The volume of each  
169 cone equals [36]:

170 
$$V_i = \frac{\pi h}{3} (R^2 + r^2 + R \cdot r) \quad (3)$$

171 where  $R$  and  $r$  are the radius of the lower and upper cross-sections, respectively, and  $h$  the  
 172 height of the cone. These three variables could be directly obtained from the bubble profiles  
 173 (depicted in **Figure 4-I**). The total volume of the bubble is the sum of the all the small cones  
 174 and the equivalent diameter could be calculated as below:

175 
$$D_{eq} = \sqrt[3]{\frac{6 \sum_{i=1}^N V_i}{\pi}} \quad (4)$$



176  
 177 **Figure 4.** Schematic diagram of the bubble profile (I) and the processing method for the  
 178 equivalent diameter of the bubble (II).

179

### 180 2.4.2 Bubble shape equation



181 As the example shown in **Figure 4**, one of the typical shapes in non-Newtonian elastic fluid is  
 182 the teardrop-like shape. It would be interesting if this kind of shape could be described by  
 183 simple parametric equations. On the geometry, there exists several mathematical curves  
 184 which are similar to the teardrop-like bubble shape, such as teardrop, simple folium and  
 185 piriform. Their parametric equations are given with corresponding profiles in **Table 2**.

186

187 **Table 2.** Approximate models of the profiles of a bubble or droplet: parametric  
 188 equation and example.

<b>Teardrop</b>	$\begin{cases} x = a \sin t \left( \sin \frac{t}{2} \right)^n \\ y = a \cos t \end{cases}$	$a=1$ $n=3$ $t \in [-\infty, +\infty]$	
-----------------	--	--	--



<p><b>Simple folium</b></p>	$\begin{cases} x = \frac{at}{1+t^2} \\ y = \frac{a}{1+t^2} \end{cases}$	<p><math>a=1</math> <math>t \in [-\infty, +\infty]</math></p> 
<p><b>Piriform</b></p>	$\begin{cases} x = \frac{a^2}{b} \cos^3 t \sin t \\ y = a \cos^2 t \end{cases}$	<p><math>a=1</math> <math>b=1</math> <math>t \in [-\infty, +\infty]</math></p> 

189

190 It should be noticed that the equations in the table can only be used to characterize the  
191 specific shapes displayed in the right-hand side of table (as shown below), i.e. the shapes  
192 with cusp at the bottom. In order to extend these equations to be used for more types of  
193 shapes like spherical, ellipsoidal and cap bubbles, a modification was implemented on the  
194 expression of the parametric equation for folium shape by adding extra variables to the  
195 equation. The appropriate expression of the parametric equation was determined through  
196 trial and error. A new parametric model is proposed as below:

$$197 \quad \begin{cases} x(t) = \frac{2x_C t}{1+t^2} \\ y(t) = \frac{y_A}{[1+\alpha t^2]^\beta} \end{cases} \quad t \in [-\infty, +\infty] \quad (5)$$

$$198 \quad E = \frac{2x_C}{y_A} \quad (6)$$

199 where:

- 200     ▪  $\alpha, \beta$  are two parameters describing the bubble shape;
- 201     ▪  $E$  is the aspect ratio;
- 202     ▪  $2x_C$  is the length of the minor axis of the bubble profile depicted in **Figure 4-I** [m];
- 203     ▪  $y_A$  is the length of the major axis of the bubble profile depicted in **Figure 4-I** [m];
- 204     ▪  $t$  is a numerical variable range between negative and positive infinity.

205 By adjusting  $\alpha$  and  $\beta$ , the modified parametric equation can be used to describe the profile of  
206 different bubble shapes that encountered in non-Newtonian fluids. The validation of the  
207 model is discussed in **Section 3.1**.

208 In a measurement, the lengths of major axis  $y_A$  and minor axis  $2x_C$  can be obtained directly  
209 from the bubble images (**Figure 3-III**). On the other hand, an optimization should be  
210 performed to determine the values of  $\alpha$  and  $\beta$ . Supposing that the edge of the bubble profile  
211 can be divided into  $N$  points, the coordinates of point  $i$  ( $x_{i,exp}, y_{i,exp}$ ) on the experimental

212 image are definite. For a pair of arbitrary values  $(\alpha, \beta)$ , from the function of ordinate in **Eq. (5)**,  
213 it has:

$$214 \quad t_i = \sqrt{\frac{1}{\alpha} [(y_{i,exp}/y_A)^{-\frac{1}{\beta}} - 1]} \quad (7)$$

215 By substituting  $t_i$  back to the function of abscissa in **Eq. (5)**, the calculated abscissa  $x_{i,cal}$   
216 can be obtained as:

$$217 \quad x_{i,cal} = \frac{2x_c t_i}{1+t_i^2} \quad (8)$$

218 The values of the parameters  $\alpha$  and  $\beta$  are then optimized by minimizing the sum of the  
219 difference at all points between the abscissa calculated with **Eq. (8)** and the one from the  
220 experiment:

$$221 \quad \sum_{i=1}^N |x_{i,cal} - x_{i,exp}| \quad (9)$$

222 The difference is then compared to the equivalent diameter and the relative deviation of the  
223 fitting result is defined as follow:

$$224 \quad err = \frac{\sum_{i=1}^N |x_{i,cal} - x_{i,exp}|}{N \cdot D_{eq}} \quad (10)$$

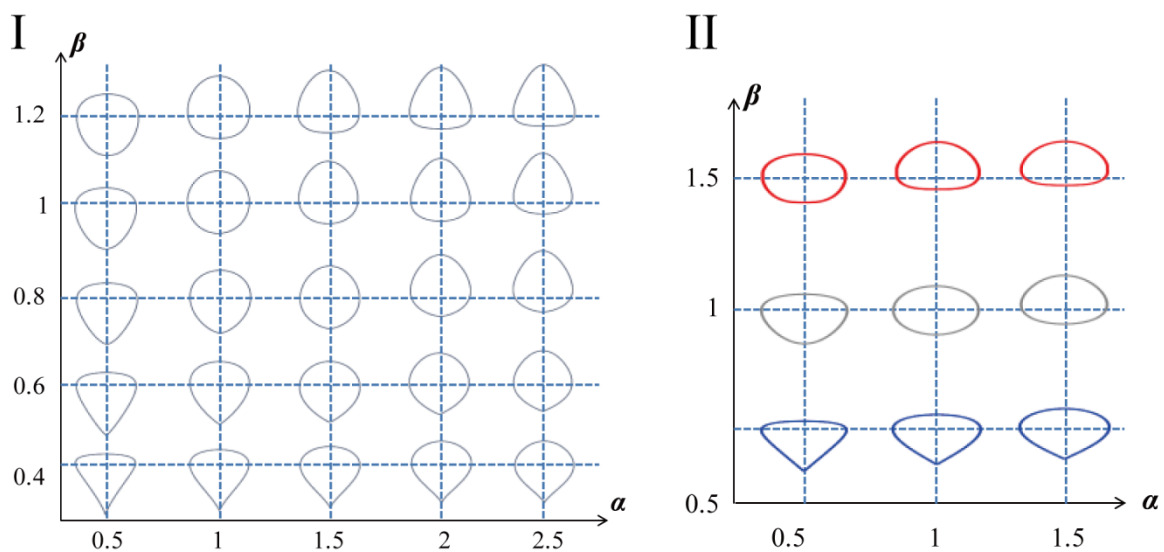
225

## 226 **3 Results and discussion**

### 227 **3.1 Validation of the parametric model**

228 Firstly, before dealing with the result from the experiment, the proposed parametric model is  
229 verified with respect to its capability for characterizing the bubble shape. According to **Eq. (5)**  
230 & **(6)**, the parametric equations for the bubble shape involve three parameters:  $\alpha$ ,  $\beta$ , and the  
231 aspect ratio,  $E$ . The evolution of the bubble shape in function of  $\alpha$  and  $\beta$  is depicted in **Figure**  
232 **5** in which the profiles of the bubbles are shown for aspect ratio  $E = 1$  (**Figure 5-I**) and  $E =$   
233  $0.5$  (**Figure 5-II**). It could be observed that the value  $E$  controls the global shape that the  
234 profile becomes more oblate with smaller value  $E$  (e.g. spherical bubble to ellipsoidal bubble).  
235 On the other hand, the parameters  $\alpha$  and  $\beta$  control the detail of the shape. The value of  $\alpha$   
236 can change the position of the minor axis (horizontal) of the bubble profiles. When the value  
237 of  $\beta$  is fixed (e.g.  $\beta = 1$ ) and  $\alpha$  increases from 0.5 to 2.5, the minor axis is moving from near  
238 the top of the bubble to the bottom of the bubble. On the other hand,  $\beta$  is related to the  
239 appearance of the cusp at the bottom of the bubble. Herein, the bubble deformation can be  
240 roughly summarized as follows:

- 241       ▪ For  $\beta < 0.6$ , there is a clear cusp at the bottom of the bubble. The typical inverted
- 242       teardrop shape appears at a high value of  $\alpha$ . (e.g. **Figure 5-I**:  $(\alpha, \beta) = (2.5, 0.4)$ ).
- 243       ▪ For  $0.6 < \beta < 0.8$ , the bubble becomes progressively rounded at the bottom and the
- 244       cusp gradually disappears as the value of  $\beta$  increases.
- 245       ▪ For  $0.8 < \beta < 1$ , there is no longer a cusp and the profile becomes more and more
- 246       rounded. The quasi-ellipsoidal bubble appears at this interval. In particular, the
- 247       circular profile (spherical bubble) and the perfectly elliptical profile (ellipsoidal bubble)
- 248       appear when the value  $\alpha$  and  $\beta$  are both equal to 1.
- 249       ▪ For  $\beta > 1$ , the bottom of the profile tends to be flat. The typical cap shape appears
- 250       when the values of  $\alpha$  and  $\beta$  are both sufficient large (e.g. **Figure 5-II**:  $\alpha = 1.5, \beta = 1.5$ ).



251

252 **Figure 5.** Evolution of the shape versus the parameters  $\alpha$  and  $\beta$  (I:  $E = 1$ , II:  $E = 0.5$ ).

253

254 Therefore, by adjusting the values of parameters  $\alpha$ ,  $\beta$  and  $E$ , the majority of the bubble

255 shapes appeared in non-Newtonian fluids can be characterized precisely. Based on the

256 parametric equations, the investigation of the bubble shape can be carried out by analyzing

257 the evolution of these parameters.

258

### 259 3.2 Bubble shape regimes

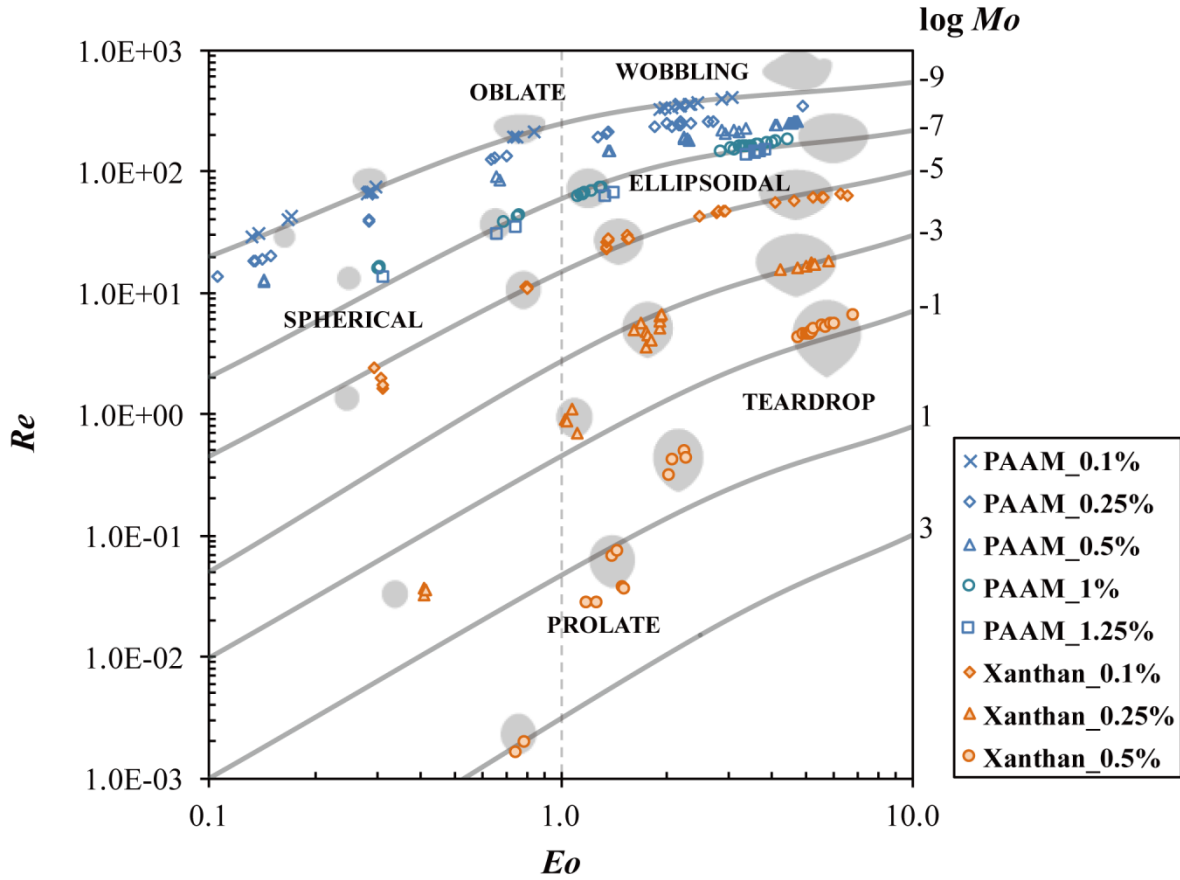
260 The resulting bubble shapes in different non-Newtonian solutions (i.e. both PAAm and

261 Xanthan gum solutions) are shown as bubble shape regime map, namely so-called Grace

262 Map, in **Figure 6**. This bubble shape regime map is plotted in terms of the dimensionless  $Re$ ,

263  $Eu$  numbers and  $\log Mo$  (dark gray curves), which can be calculated as defined in **Eq.(11)**-

264 (13), and the typical bubble shapes (gray patterns in the background) extracted from the raw  
 265 images (Figure 3-III) are also depicted near the corresponding experimental points.



266

267 **Figure 6.** Shape regime map (namely Grace Map) for bubbles in PAAm and Xanthan gum  
 268 solutions (dark gray curves:  $\log Mo$ ; gray patterns in the background: typical bubble shape  
 269 near the corresponding experimental points).

270

271 
$$Eo = \frac{\rho g D_{eq}^2}{\sigma} \quad (11)$$

272 
$$Re = \frac{\rho U D_{eq}}{\mu} \quad (12)$$

273 
$$Mo = \frac{g \mu^4}{\rho \sigma^3} \quad (13)$$

274 In PAAm solutions, the range of  $Mo$  number is relatively small ( $-9 < \log Mo < -7$ ) within the  
 275 concentration range of study (0.1% - 1.25% wt.). The data covers the spherical bubble and  
 276 the ellipsoidal bubble regimes. When increasing  $Eo$  and  $Re$ , the bubble becomes bigger and  
 277 the shape changes from spherical to ellipsoidal. Regarding the concentration of the solution,  
 278 it can be seen that the  $Re$  increases in a dilute solution, making the bubble shape become  
 279 more oblate and even causing wobbling due to the surface oscillation.

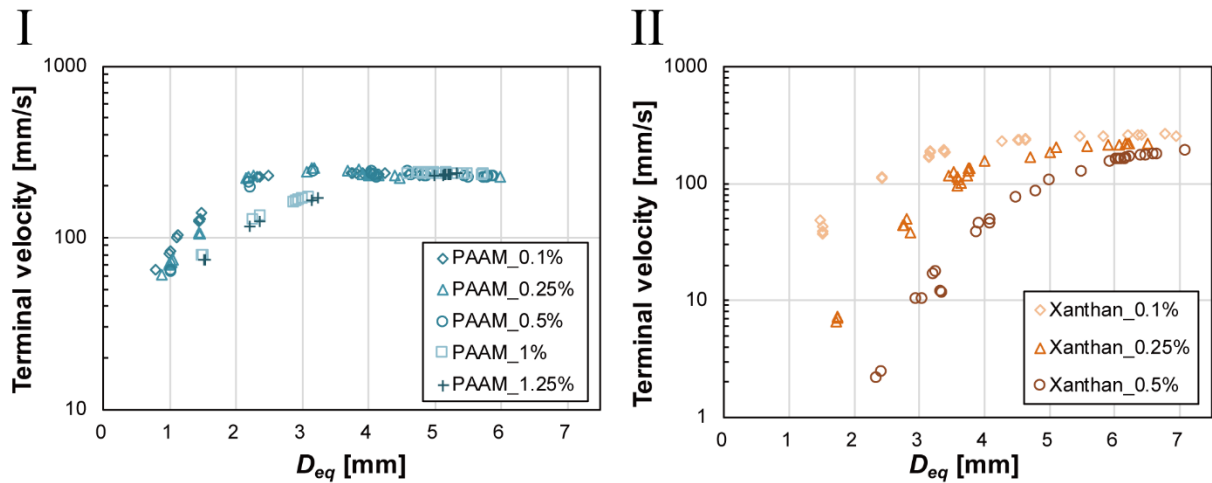
280 In Xanthan solutions, the range of  $Mo$  number is larger ( $-9 < \log Mo < 3$ ) under the investigated  
281 concentration (0.1% - 0.5% wt.). The data covers not only the spherical and ellipsoidal  
282 bubbles but also the prolate and teardrop ones. A similar tendency is found for the bubble  
283 deformation as in the PAAm solutions. In particular, the cusp appears for high  $Eo$  number  
284 ( $Eo > 1$ ) and becomes more significant with the increase of the solution concentration or for  
285 lower  $Re$  number. Under this condition, the bubble is also elongated vertically, which is  
286 uncommon in Newtonian fluids.

287 Compared with the Grace map given by Clift et al. [37] for bubble shapes in Newtonian fluids,  
288 the regimes of the spherical bubble and the ellipsoidal bubble in the present study are  
289 consistent when  $Re > 1$ . However, the bubble shapes are invariably spherical when  $Re < 1$ ,  
290 which are contrary to those in non-Newtonian fluids. In fact, in non-Newtonian fluids, as the  
291 bubble velocity could be extremely low due to the complex rheological properties of the  
292 solution, relatively smaller values of  $Re$  number should be considered, namely  $Re$  ranging  
293 from 0.001 to 1 in this study. Within this range, the prolate bubble and teardrop bubble can  
294 also be visualized while the spherical bubble appears only for low  $Eo$  number ( $Eo < 1$ ).

295

### 296 **3.3 Bubble velocity**

297 Concerning the bubble terminal velocity, as shown in **Figure 7**, for both types of the solutions,  
298 it first increases with the bubble size then tends to be constant. Although the velocity curves  
299 at different concentrations differ more from each other for Xanthan solutions, this evolution  
300 and the final constant velocity do not depend on the type of solution or the concentration of  
301 the solute. It could be derived that, in a highly viscous Xanthan solution, the bubble rises  
302 much more slowly and needs to attain the final constant velocity in a bigger size. In particular,  
303 it exists a remarkable difference between the curves of the three lower concentrations of  
304 PAAm solutions and those of the two higher concentrations. The reason is that, in the dilute  
305 PAAm solutions (0.1%- 0.5% wt), the bubble shape is less stable with the surface oscillation,  
306 which leads to the reduction of the viscosity around the bubble due to the shear thinning  
307 property. On the other hand, when a bubble is rising in a concentrated PAAm solution (1%-  
308 1.25% wt), the surface oscillation no longer exists due to the higher viscosity. The bubble  
309 thus encounters more resistance and its velocity is much slower. Moreover, there is no  
310 evident velocity discontinuity under our experimental conditions indicating that the bubble  
311 terminal velocity could be less influenced by the bubble shape deformation (from ellipsoidal  
312 to inverted teardrop). This result is consistent with the literature [38], in which the same  
313 behavior of rising bubbles was found in CMC solutions and Xanthan gum solutions.



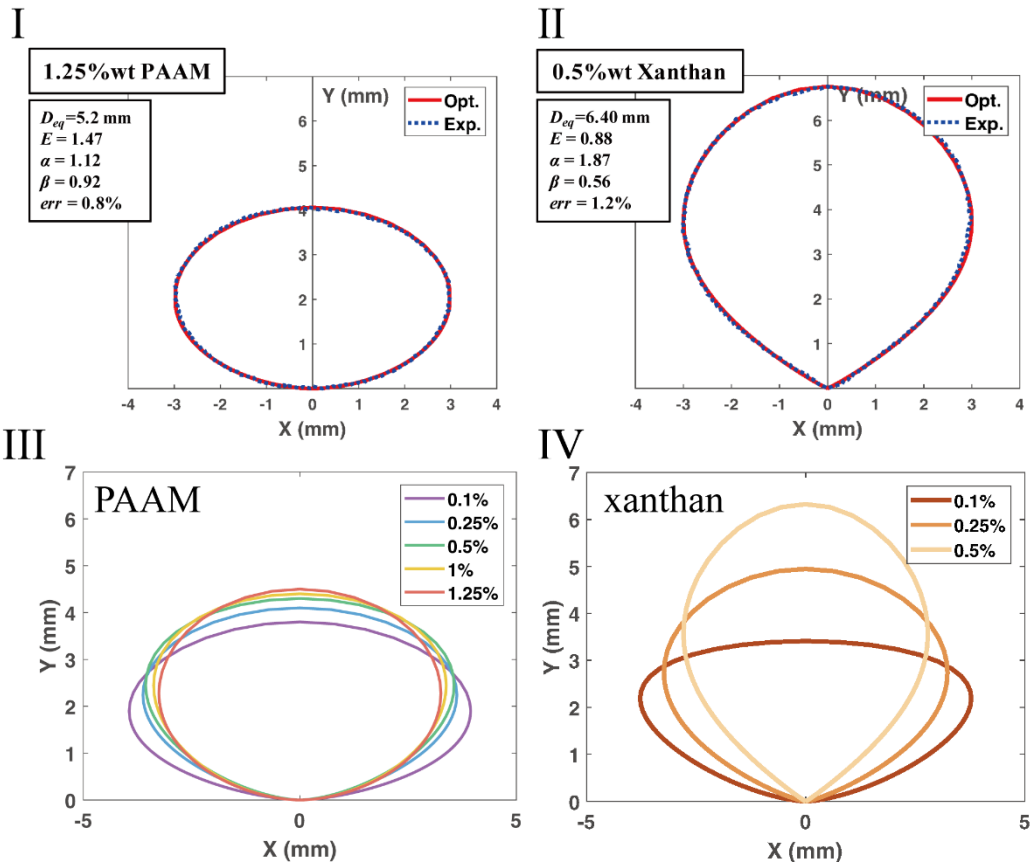
314

315 **Figure 7.** Relationship between bubble rising velocity and bubble size ( $D_{eq} = 0.7\sim 7$  mm) in  
 316 PAAm (I) and Xanthan gum solutions (II).

317

### 318 3.4 Bubble shape parameters

319 To better analyze the bubble shape, the bubble profile was fitted by the parametric models  
 320 introduced in **Section 2.4.2**. It should be noticed that the bubble shape is assumed to be  
 321 stable without surface oscillation. The data for big bubble ( $D_{eq} > 6$  mm) rising in dilute PAAm  
 322 solution (0.1%- 0.5% wt) has been eliminated due to the non-negligible surface oscillation.  
 323 Two typical fitting results, chosen for single bubbles in Xanthan gum and PAAm solutions,  
 324 are shown in **Figure 8-I & II**, where the black dots depict the origin profile of the bubble and  
 325 the red line is the fitting profile with the values of  $\alpha$  and  $\beta$  given alongside. It can be seen that  
 326 whether the bubble has a teardrop or an ellipsoidal shape, the deviation between the  
 327 experimental points and the fitting points is small. The deviation defined in **Eq. (10)** is in a  
 328 magnitude smaller than 3% for all the cases. To ensure the validity of the bubble  
 329 characterization result, fitting data with an error of more than 2% was eliminated. An example  
 330 of the averaged fitting results of the bubble shapes in both PAAm and Xanthan solutions  
 331 under different concentrations are shown in **Figure 8-III & IV**. It can be observed that under  
 332 the same operational condition for bubble generation (i.e. the size of nozzle and the air flow  
 333 rate), the sizes and shapes of bubbles depend on the type and concentration of the solutes  
 334 (i.e. PAAm and Xanthan gum). In addition, the evolution of the bubble shapes given by the  
 335 model is consistent with the original bubble shapes depicted in **Figure 6**.



336

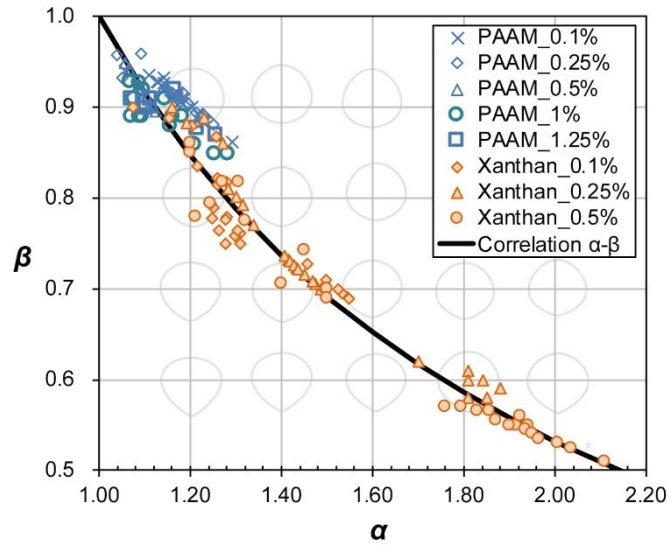
337 **Figure 8.** Examples of the bubble profiles and the fitting ones by Eq. (5) & (6) in PAAm (I, III)  
 338 and Xanthan solutions (II, IV) under different concentrations. (The bubbles are injected by  
 339 the nozzle with a caliber of 1 mm at a flow rate of 10  $\mu\text{L/h}$ ).

340

341 It can be seen from **Figure 8-III & IV** that in PAAm solution, the size of the bubble slightly  
 342 changes, while the shape becomes more and more rounded for higher concentrations,  
 343 namely, from an oblate bubble to a general ellipsoidal bubble. In contrast, in Xanthan  
 344 solutions, the major axis (vertical) of the bubble increases as the concentration of Xanthan  
 345 increases, as well as the bubble deforms from an oblate ellipsoid to an oblate teardrop and  
 346 then turns to an elongate teardrop.

347 For a single bubble, a pair of parameters ( $\alpha$ ,  $\beta$ ) could be obtained from the fitting result. In  
 348 **Figure 9**, the relationship between the bubble shape parameters ( $\alpha$  and  $\beta$ ) are depicted for  
 349 bubbles in both PAAm and Xanthan gum solutions. The corresponding bubble profiles (light  
 350 gray outline) are also displayed at the positions of values  $\alpha$  and  $\beta$ . In this figure, the delicate  
 351 changes of bubble shape can be visualized and quantified, which is difficult to achieve simply  
 352 by using the aspect ratio. For PAAm solutions, the data are concentrated in the range of  $1 < \alpha$   
 353  $< 1.2$  and  $0.8 < \beta < 1$ , suggesting that the bubble is spherical or ellipsoidal, while, for the  
 354 Xanthan solution, the range of these two parameters is much larger. As the parameter  $\alpha$   
 355 increases, the value of  $\beta$  decreases gradually. As interpreted in **Section 2.4.2**, the cusp of

356 the bubble appears when  $\beta < 0.6$  and it becomes sharper when  $\beta$  continues to decrease.  
 357 The result of the Xanthan gum cases shows good agreement with this evolution.



358  
 359 **Figure 9.** Relationship between the bubble shape parameters ( $\alpha$  and  $\beta$ ) in both PAAm and  
 360 Xanthan solutions under different concentrations.

361  
 362 It is found that the relationship between  $\alpha$  and  $\beta$  could be correlated by a power-law function,  
 363 which is expressed as below:

364 
$$\alpha^{0.85}\beta = 1 \tag{14}$$

365 In the range investigated in this study ( $-9 < \log Mo < 3$ ), the accuracy of this correlation is  
 366 acceptable, with a determination coefficient  $r^2 > 95\%$ . It can be seen from **Figure 9** that the  
 367 curve of **Eq. (14)** passes the point  $(\alpha, \beta) = (1, 1)$ , which indicates a perfect spherical bubble  
 368 (or an ellipsoidal bubble when  $E \neq 1$ ). Thanks to **Eq. (14)**, it is possible to characterize the  
 369 bubble shape with only one parameter (either  $\alpha$  or  $\beta$ ). In the next section, only the parameter  
 370  $\beta$  is taken into account.

371  
 372 **3.5 Prediction of bubble shape**

373 It is known from **Section 3.1** that the aspect ratio  $E$  roughly describes the bubble shape while  
 374 the parameter  $\alpha$  and  $\beta$  characterize the details of bubble deformation. As mentioned in the  
 375 introduction that a lot of research has been carried out for predicting the aspect ratio  $E$  for  
 376 bubbles in different liquids, we will focus on the discussion of the bubble shape parameter  $\beta$ .

377 Depending on the value of  $\beta$ , bubble shape changes from ellipsoidal (without cusp) to  
 378 teardrop (with cusp). Some existed research attempts to explain the appearance of the cusp



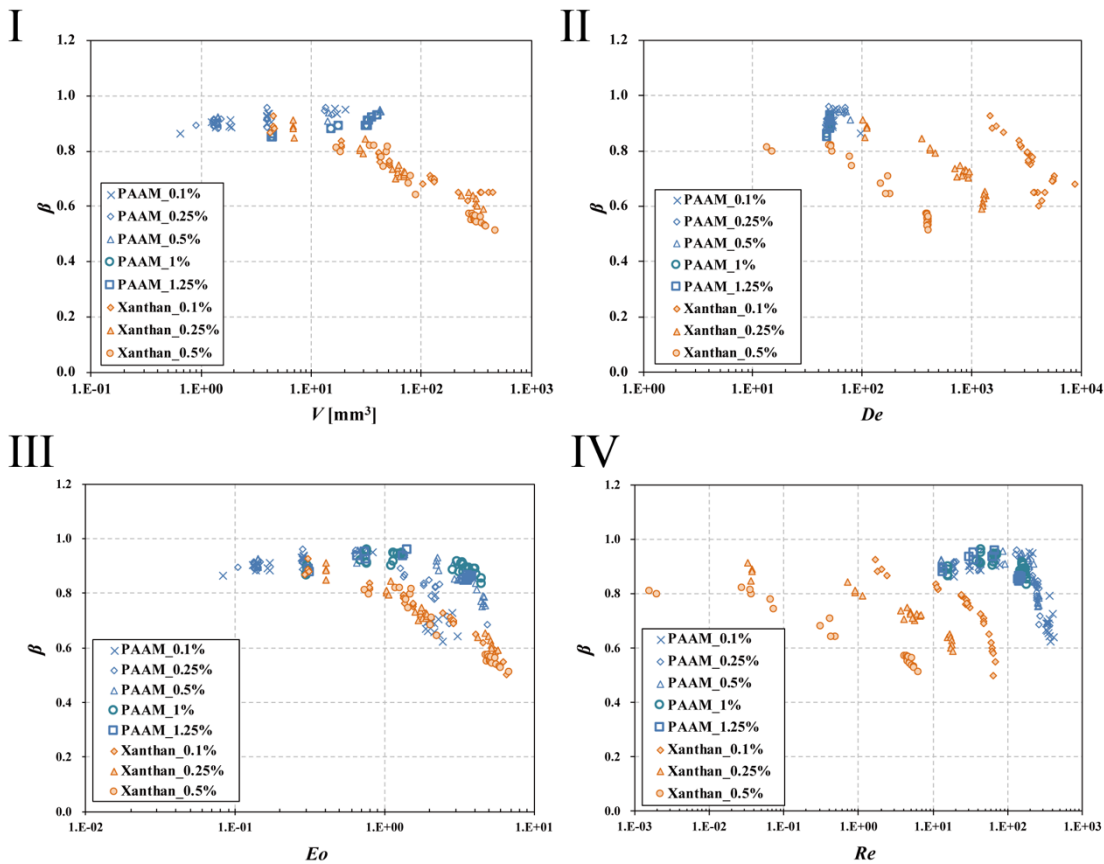
379 theoretically and most of the authors support the reason that the majority of non-Newtonian  
 380 fluids are composed of long-chain molecules and possess viscoelasticity [39,40]. To quantify  
 381 the elasticity of the fluid, the Deborah number is utilized to compare the relaxation time of the  
 382 fluid to the time scale of observation [41]:

$$383 \quad De = \frac{\lambda U}{Deq} = \lambda \dot{\gamma} \quad (15)$$

384 In our study, the observation time is estimated that it is equal to the characteristic time of the  
 385 motion (i.e. the equivalent diameter of the bubble divided by the bubble rising velocity). Since  
 386 this characteristic time of the motion is relatively short comparing with the relaxation time of  
 387 the fluid, the magnitude of calculated  $De$  number in this study may be higher than the  
 388 literature [42]. Nonetheless, it can still be used to compare the elastic levels for the  
 389 investigated fluids.

390 Since the cusp could now be quantified by the parameter  $\beta$ , the evolution of  $\beta$  is analyzed in  
 391 terms of the bubble size ( $V$ ) and various dimensionless numbers ( $De$ ,  $Eo$ ,  $Re$ ), shown as in  
 392 **Figure 10**.

393



394

395 **Figure 10.** The evolution of parameter  $\beta$  in terms of the bubble size ( $V$ ) and various  
396 dimensionless numbers ( $De$ ,  $EO$ ,  $Re$ ) in PAAm and Xanthan solutions under different  
397 concentrations.

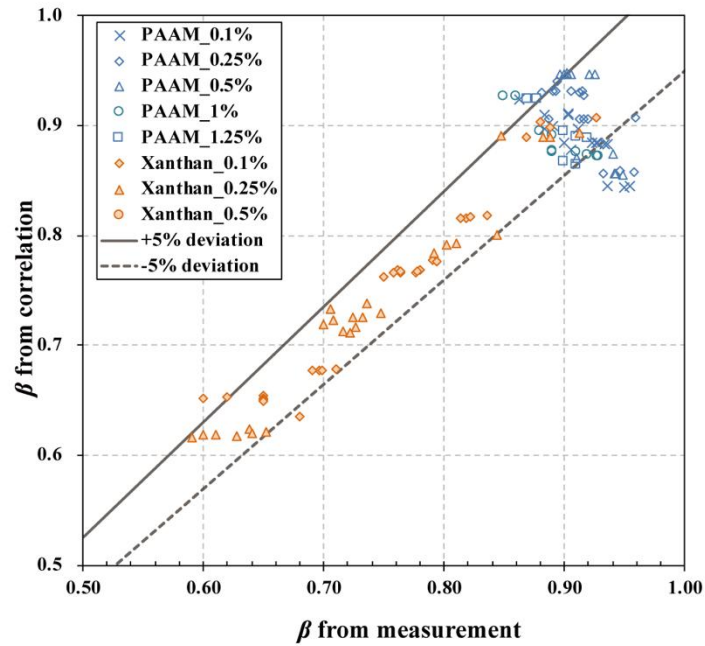
398

399 It can be obtained from **Figure 10** that: (1) for larger bubbles, the velocity of the bubble  
400 increases then the bubble begins to deform and becomes less rounded when the  
401 contribution of inertial force and buoyancy is stronger than the surface tension and viscous  
402 force. (2)  $\beta$  decreases with higher elasticity of the solution in most investigated range except  
403 for some PAAm which are relatively less elastic. If the bubble moves too fast, the liquid  
404 cannot fill the space in the rear of the bubble immediately. Hence this space is still occupied  
405 by the gas and pressed by the long-chain liquid molecule from the side, leading to a little  
406 cusp forming in the rear of the bubble. (3) In the evolution of  $\beta - De$  and  $\beta - Re$ , the evolution  
407 of the value  $\beta$  under three concentrations is quite dispersed. This result might be caused by  
408 the different shear-thinning level of the solutions as the shear-thinning property is also a  
409 reason for the deformation of the bubble [43].

410 The data in **Figure 10** are too scattered for a general law to be obtained. Hence multiple  
411 influencing factors are considered instead of one. By analogy with the analysis of aspect ratio,  
412 the investigation was carried out for the evolution of  $\beta$  with different pairs of dimensionless  
413 numbers as well as the shear-thinning property which can be roughly quantified by the power  
414 index  $n$  (Eq. (1)). After testing several functions, the following correlation was proposed to fit  
415 the experimental data:

$$416 \quad \beta = n - 0.11De^{0.19}EO^{0.11} + 0.80 \quad (16)$$

417 This equation is correlated to the result depicted in **Figure 10** as  $\beta$  decreases monotonically  
418 with high  $De$ ,  $EO$  numbers and the shear-thinning levels. The comparison between parameter  
419  $\beta$  predicted by **Eq. (16)** and the experimental ones is shown in **Figure 11**. It can be seen that,  
420 under the range of this study ( $-9 < \log Mo < 3$ ), the prediction quality of parameter  $\beta$  in both  
421 PAAm and Xanthan gum solutions is satisfactory. Relatively large deviation appears at high  
422 values of  $\beta$  due to the wobbling of the bubble rising in dilute PAAm solutions. The fitting  
423 result has a coefficient of determination ( $r^2$ ) higher than 95%.



424

425 **Figure 11.** Comparison result between parameter  $\beta$  from correlation (Eq.(16)) and  $\beta$  from  
 426 measurement in PAAM and Xanthan gum solutions.

427

#### 428 **4 Conclusions**

429 In this paper, various single air bubbles rising in stagnant non-Newtonian fluids  
 430 (polyacrylamide, Xanthan gum) were investigated by high-speed photography. The shapes of  
 431 the bubbles from spherical to inverted teardrop can be characterized with good accuracy by  
 432 parametric equations which contain the aspect ratio ( $E$ ) and two shape parameters ( $\alpha, \beta$ ).  
 433 Based on this method, the various impacts on the bubble shape can be quantified by  
 434 studying the evolution of the three parameters as a function of bubble size, bubble velocity,  
 435 multiple dimensionless numbers ( $Re, Eo$ , etc.) and the property of the fluids. Within the range  
 436 investigated here ( $-9 < \log Mo < -7$ ), it is found that the cusp of the bubble (quantified by  $\beta$ ) is  
 437 related to the viscoelasticity as well as the shear-thinning level of the solutions. A simple  
 438 correlation is then proposed to predict the parameter  $\beta$ . Since the parametric equations are  
 439 capable to characterize most of observed shapes (including cap bubble), this method can be  
 440 applied to bigger bubble or droplets in complex Newtonian and non-Newtonian fluids.

441

442 **Symbols used**

$D_{eq}$	[mm]	equivalent diameter
$E$	[-]	aspect ratio
$Eo$	[-]	Eötvös number
$g$	[m·s <sup>-2</sup> ]	gravitational acceleration
$Mo$	[-]	Morton number
$n$	[-]	power index / shear-thinning level
$P$	[mm]	perimeter
$r^2$	[-]	determination coefficient
$Re$	[-]	Reynolds number
$S$	[mm <sup>2</sup> ]	surface area
$t$	[-]	numerical variable
$Ta$	[-]	Tadaki number
$U_x$	[mm·s <sup>-1</sup> ]	oscillating velocity
$U_y$	[mm·s <sup>-1</sup> ]	rising velocity
$V$	[mm <sup>3</sup> ]	Bubble volume
$We$	[-]	Weber number
$X_{i,cal}$	[mm]	abscissa by calculation
$X_{i,exp}$	[mm]	abscissa by experiment
$x_C$	[mm]	half-length of major axis
$y_A$	[mm]	length of minor axis

**Greek Symbols**

$\alpha$	[-]	bubble shape parameter
$\beta$	[-]	bubble shape parameter
$\dot{\gamma}$	[s <sup>-1</sup> ]	shear rate
$\lambda$	[s]	relaxation time
$\mu$	[Pa·s]	dynamic viscosity
$\rho$	[kg·m <sup>-3</sup> ]	density
$\sigma$	[N·m <sup>-1</sup> ]	surface tension

443

444 **Acknowledgments**

445 The financial assistance provided for Feishi. XU by the China Scholarship Council is  
446 gratefully acknowledged. The federation FERMAT is also thanked for its leading-edge  
447 material support.

448

449 **References**

450 [1] R.P. Chhabra, Bubbles, Drops, and Particles in Non-Newtonian Fluids, Second  
451 Edition, 2 edition, CRC Press, 2006.

452 [2] F. Xu, A. Cockx, G. Hébrard, N. Dietrich, Mass Transfer and Diffusion of a Single  
453 Bubble Rising in Polymer Solutions, Ind. Eng. Chem. Res. (2018).

454 doi:10.1021/acs.iecr.8b03617.

455 [3] J. Grace, T. Wairegi, T.H. Nguyen, Shapes and Velocities of Single Drops and  
456 Bubbles Moving Freely Through Immiscible Liquids, *Trans Inst Chem Eng.* 54 (1976) 167–  
457 173.

458 [4] S. Anwar, Lattice Boltzmann modeling of buoyant rise of single and multiple bubbles,  
459 *Comput. Fluids.* 88 (2013) 430–439. doi:10.1016/j.compfluid.2013.09.015.

460 [5] J. Hua, J.F. Stene, P. Lin, Numerical simulation of 3D bubbles rising in viscous liquids  
461 using a front tracking method, *J. Comput. Phys.* 227 (2008) 3358–3382.

462 doi:10.1016/j.jcp.2007.12.002.

463 [6] Z. Yu, H. Yang, L.-S. Fan, Numerical simulation of bubble interactions using an  
464 adaptive lattice Boltzmann method, *Chem. Eng. Sci.* 66 (2011) 3441–3451.

465 doi:10.1016/j.ces.2011.01.019.

466 [7] L. Böhm, T. Kurita, K. Kimura, M. Kraume, Rising behaviour of single bubbles in  
467 narrow rectangular channels in Newtonian and non-Newtonian liquids, *Int. J. Multiph. Flow.*

468 65 (2014) 11–23. doi:10.1016/j.ijmultiphaseflow.2014.05.001.

469 [8] X. Frank, H.Z. Li, D. Funfschilling, F. Burdin, Y. Ma, Bubble Motion in Non-Newtonian  
470 Fluids and Suspensions, *Can. J. Chem. Eng.* 81 (2003) 483–490.

471 doi:10.1002/cjce.5450810321.

472 [9] X. Frank, J.-C. Charpentier, Y. Ma, N. Midoux, H.Z. Li, A Multiscale Approach for  
473 Modeling Bubbles Rising in Non-Newtonian Fluids, *Ind. Eng. Chem. Res.* 51 (2012) 2084–

474 2093. doi:10.1021/ie2006577.

475 [10] N.M.S. Hassan, M.M.K. Khan, D.W. Rackemann, An experimental study of bubble  
476 rise characteristics in non-Newtonian (power-law) fluids, 16th Australas. Fluid Mech. Conf.

477 AFMC. (2007). <http://acquire.cqu.edu.au:8080/vital/access/manager/Repository/cqu:2807>

478 (accessed January 31, 2017).

479 [11] N.M.S. Hassan, M.M.K. Khan, M.G. Rasul, D.W. Rackemann, Bubble Rise Velocity  
480 and Trajectory in Xanthan Gum Crystal Suspension, *Appl. Rheol.* 20 (2010) 65102.

481 [12] L. Zhang, C. Yang, Z.-S. Mao, Numerical simulation of a bubble rising in shear-  
482 thinning fluids, *J. Non-Newton. Fluid Mech.* 165 (2010) 555–567.

483 doi:10.1016/j.jnnfm.2010.02.012.

484 [13] D. Dekée, R.P. Chhabra, A photographic study of shapes of bubbles and  
485 coalescence in non-Newtonian polymer solutions, *Rheol. Acta.* 27 (1988) 656–660.

486 doi:10.1007/BF01337462.

- 487 [14] D. Dekée, P.J. Carreau, J. Mordarski, Bubble velocity and coalescence in viscoelastic  
488 liquids, *Chem. Eng. Sci.* 41 (1986) 2273–2283. doi:10.1016/0009-2509(86)85078-3.
- 489 [15] D. Funfschilling, H.Z. Li, Effects of the Injection Period on the Rise Velocity and  
490 Shape of a Bubble in a Non-Newtonian Fluid, *Chem. Eng. Res. Des.* 84 (2006) 875–883.  
491 doi:10.1205/cherd.01229.
- 492 [16] N. Dietrich, G. Hebrard, Visualisation of gas-liquid mass transfer around a rising  
493 bubble in a quiescent liquid using an oxygen sensitive dye, *Heat Mass Transf.* (2018) 1–9.  
494 doi:10.1007/s00231-018-2297-3.
- 495 [17] N. Dietrich, K. Wongwailikhit, M. Mei, F. Xu, F. Felis, A. Kherbeche, G. Hébrard, K.  
496 Loubière, Using the “Red Bottle” Experiment for the Visualization and the Fast  
497 Characterization of Gas–Liquid Mass Transfer, *J. Chem. Educ.* (2019).  
498 doi:10.1021/acs.jchemed.8b00898.
- 499 [18] A. Kherbeche, M. Mei, M.-J. Thoraval, G. Hébrard, N. Dietrich, Hydrodynamics and  
500 gas-liquid mass transfer around a confined sliding bubble, *Chem. Eng. J.* (2019).  
501 doi:10.1016/j.cej.2019.04.041.
- 502 [19] D.W. Moore, The rise of a gas bubble in a viscous liquid, *J. Fluid Mech.* 6 (1959)  
503 113–130. doi:10.1017/S0022112059000520.
- 504 [20] T. Tadaki, S. Maeda, On the Shape and Velocity of Single Air Bubbles Rising in  
505 Various Liquids, *Chem. Eng.* 25 (1961) 254–264. doi:10.1252/kakoronbunshu1953.25.254.
- 506 [21] T.D. Taylor, A. Acrivos, On the deformation and drag of a falling viscous drop at low  
507 Reynolds number, *J. Fluid Mech.* 18 (1964) 466–476. doi:10.1017/S0022112064000349.
- 508 [22] R.M. Wellek, A.K. Agrawal, A.H.P. Skelland, Shape of liquid drops moving in liquid  
509 media, *AIChE J.* 12 (1966) 854–862. doi:10.1002/aic.690120506.
- 510 [23] I.A. Vakhrushev, G.I. Efremov, Interpolation formula for computing the velocities of  
511 single gas bubbles in liquids, *Chem. Technol. Fuels Oils.* 6 (1970) 376–379.  
512 doi:10.1007%2fBF01171684.
- 513 [24] L.-S. Fan, K. Tsuchiya, *Bubble Wake Dynamics in Liquids and Liquid-Solid*  
514 *Suspensions*, Butterworth-Heinemann, Boston, Mass, 1990.
- 515 [25] F. Raymond, J.-M. Rosant, A numerical and experimental study of the terminal  
516 velocity and shape of bubbles in viscous liquids, *Chem. Eng. Sci.* 55 (2000) 943–955.  
517 doi:10.1016/S0009-2509(99)00385-1.
- 518 [26] K. Sugihara, T. Sanada, M. Shirota, M. Watanabe, Behavior of single rising bubbles  
519 in superpurified water, *KAGAKU KOGAKU RONBUNSHU.* 33 (2007) 402–408.

- 520 [27] D. Legendre, R. Zenit, J.R. Velezcordero, On the deformation of gas bubbles in  
521 liquids, *Phys. Fluids*. 24 (2012) 043303.
- 522 [28] G. Kelbaliyev, K. Ceylan, Development of New Empirical Equations for Estimation of  
523 Drag Coefficient, Shape Deformation, and Rising Velocity of Gas Bubbles or Liquid Drops,  
524 *Chem. Eng. Commun.* 194 (2007) 1623–1637. doi:10.1080/00986440701446128.
- 525 [29] L. Liu, H. Yan, G. Zhao, Experimental studies on the shape and motion of air bubbles  
526 in viscous liquids, *Exp. Therm. Fluid Sci.* 62 (2015) 109–121.  
527 doi:10.1016/j.expthermflusci.2014.11.018.
- 528 [30] W. Myint, S. Hosokawa, A. Tomiyama, Shapes of Single Drops Rising Through  
529 Stagnant Liquids, *J. Fluid Sci. Technol.* 2 (2007) 184–195. doi:10.1299/jfst.2.184.
- 530 [31] H. Yan, J. Zhao, Experimental study on shape and rising behavior of single bubble in  
531 stagnant water, *J. Cent. South Univ. Sci. Technol.* 47 (2016) 2513–2520.
- 532 [32] R.L. Davidson, *Handbook of water-soluble gums and resins*, McGraw-Hill, 1980.
- 533 [33] R. Byron Bird, P.J. Carreau, A nonlinear viscoelastic model for polymer solutions and  
534 melts-I, *Chem. Eng. Sci.* 23 (1968) 427–434. doi:10.1016/0009-2509(68)87018-6.
- 535 [34] P.J. Carreau, I.F. MacDonald, R.B. Bird, A nonlinear viscoelastic model for polymer  
536 solutions and melts-II, *Chem. Eng. Sci.* 23 (1968) 901–911. doi:10.1016/0009-  
537 2509(68)80024-7.
- 538 [35] N. Dietrich, *Étude locale et expérimentale des phénomènes interfaciaux*,  
539 Vandoeuvre-les-Nancy, INPL, 2008. <http://www.theses.fr/2008INPL078N> (accessed  
540 September 20, 2016).
- 541 [36] J.W. Harris, H. Stöcker, *Handbook of Mathematics and Computational Science*, 1998  
542 edition, Springer, New York, 1998.
- 543 [37] R. Clift, J.R. Grace, M.E. Weber, *Bubbles, Drops, and Particles*, Dover Publications,  
544 New York, 1978.
- 545 [38] S. Amirnia, J.R. de Bruyn, M.A. Bergougnou, A. Margaritis, Continuous rise velocity of  
546 air bubbles in non-Newtonian biopolymer solutions, *Chem. Eng. Sci.* 94 (2013) 60–68.  
547 doi:10.1016/j.ces.2013.02.032.
- 548 [39] S.M. Barnett, A.E. Humphrey, M. Litt, Bubble motion and mass transfer in non-  
549 Newtonian fluids, *AIChE J.* 12 (1966) 253–259.
- 550 [40] R. Zenit, J.J. Feng, Hydrodynamic Interactions Among Bubbles, Drops, and Particles  
551 in Non-Newtonian Liquids, *Annu. Rev. Fluid Mech.* 50 (2018) 505–534. doi:10.1146/annurev-  
552 fluid-122316-045114.

- 553 [41] M. Reiner, The Deborah Number, *Phys. Today*. 17 (1964) 62. doi:10.1063/1.3051374.
- 554 [42] R.P. Chhabra, *Non-Newtonian Fluids: An Introduction*, in: *Rheol. Complex Fluids*,  
555 Springer Science & Business Media, 2010: pp. 3–34.  
556 [https://link.springer.com/chapter/10.1007/978-1-4419-6494-6\\_1](https://link.springer.com/chapter/10.1007/978-1-4419-6494-6_1) (accessed February 22,  
557 2019).
- 558 [43] M. Warshay, E. Bogusz, M. Johnson, R. C. Kintner, Ultimate velocity of drops in  
559 stationary liquid media, *Can. J. Chem. Eng.* 37 (1959) 29–36. doi:10.1002/cjce.5450370107.
- 560